Lawrence Berkeley National Laboratory

Title
Microscale mechanical property variations of Al-substituted LLZO: insights from compression testing and molecular dynamics simulations

Permalink
https://escholarship.org/uc/item/2hv4s8q8

Authors
Moon, Jaron V
Sakir, Md Takmil
Go, Wooseok
et al.

Publication Date
2024

DOI
10.1039/d4ta03596h

**Copyright Information**

Peer reviewed

Microscale mechanical property variations of Al-substituted LLZO: insights from compression testing and molecular dynamics simulations

Authors: Jaron V. Moon[a], Md Takmil Sakir[c], Wooseok Go[b], Rui Xie[a], Michael C. Tucker[b], Marca Doeff[b], Haoran Wang[c], Roseanne Warren[a]*

a. University of Utah, Department of Mechanical Engineering, 1495 E 100 S, Salt Lake City, UT 84112

b. Energy Storage and Distributed Resources Division, Lawrence Berkeley National Laboratory, Berkeley, CA 94720

c. Mechanical and Aerospace Engineering, Utah State University, Logan, UT 84322

*Corresponding Author – roseanne.warren@utah.edu

Graphical Abstract
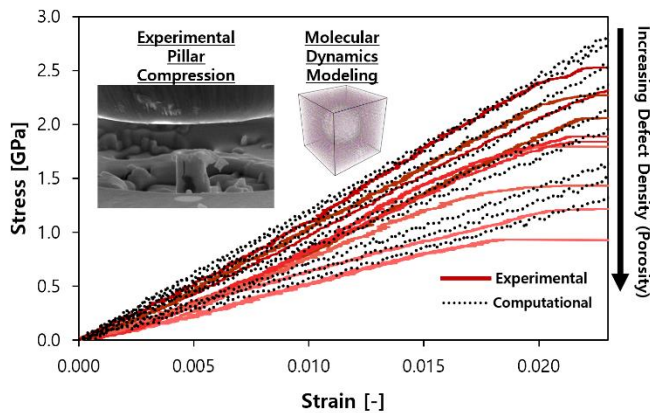
Abstract (191 words)

Ceramic solid electrolytes based on LLZO ($Li_7La_3Zr_2O_{12}$) are promising candidates for all-solid-state batteries due to their high ionic conductivity and good apparent stability *vs*. lithium metal, however they are prone to mechanical failure. Lithium metal intrusions, alongside cell stack pressure, transition polycrystalline solid electrolyte grains into a compressed state that promotes crack propagation and fracture. This work examines the mechanical response of Al-substituted LLZO to compressive forces by measuring ultimate strength under pillar compression with a flat punch tip. Failure modes characterized by *in-situ* scanning electron microscopy show diverse splitting patterns arising from internal porosity, grain boundaries, and slip planes. Large correlated variations in compressive strength (0.93-2.63 GPa) and Young's modulus (72.1-150.97 GPa) are observed across microscale regions of the solid electrolyte. Molecular dynamics simulations of LLZO with different porosities describe the variation of compressive strength and Young's modulus, and enable a microscale porosity model to be fit accounting for Young's modulus reduction across the solid electrolyte. Overall, the results indicate the importance of microscale mechanical testing of ceramic solid electrolytes to identify preferential sites for mechanical degradation and Li intrusion, and ensure the robust design of all-solid-state lithium metal batteries.

Keywords:

Introduction

Lithium lanthanum zirconium oxide (LLZO) is a garnet ceramic solid electrolyte (SE) with great promise for use in all-solid-state lithium metal batteries. Its advantages include enabling the use of a lithium metal anode with a high theoretical specific capacity (3860 mAhg⁻¹), and improved safety in the absence of flammable electrolytes [1]. In an all-solid-state battery, the SE is subject to myriad compressive and tensile stresses (Figure 1a). Although LLZO is a ceramic material with a large Young's modulus (~150 GPa) and high hardness (~6-11 GPa), it is prone to failure from short-circuiting due to dendrite propagation through the SE [2]. Prior research has shown the susceptibility of ceramic SEs to lithium metal penetration *via* inter- and intragranular mechanisms [3], [4]. Many studies have investigated the propensity for lithium metal to nucleate at voids within the SE [5], producing tensile stresses that induce SE failure by mode I crack propagation [6] (Figure 1b). In addition to tensile stresses, LLZO polycrystalline grains may also transition into a compressed state during lithium intrusion into the SE, with stress concentrations large enough to initiate crack propagation parallel to the direction of compressive loading [7] (Figure 1c). Increasing cell stack pressure has been shown to allow better cycling of solid-state batteries by improving contact between the electrodes and the SE [8]˙[9]. The introduction of cell stack pressure is another probable cause of SE failure in compression (Figure 1d).

The plausibility that large compressive stresses exist within the SE during cycling offers the need to further study the mechanical response of LLZO under compression. Instrumented indentation testing of LLZO to-date has been limited to reports of bulk sample Young's modulus, hardness, and fracture toughness [10] (Supporting Information Table S1 [11]-[14]). LLZO is a brittle material with low deformability and a tendency to fracture under compressive loading. Compressive strength is a material property that describes the stress at which a material will fail

under uniaxial compression; compressive strain describes the corresponding strain at failure. Despite the importance of compressive strength and strain for ceramic solid electrolyte performance, to-date no reported work has attempted to define these properties of LLZO experimentally or computationally.

A further question requiring investigation is the extent to which LLZO mechanical properties, including Young's modulus and compressive strength, may vary spatially across the SE. We hypothesize that microscale property changes arising from defects and/or density variations within the SE produce significant effects on the mechanical properties of LLZO. Microscale property variations are highly applicable to battery materials, as Li nucleation occurs on such length scales. Defects may present in LLZO as localized porosity, pre-existing cracks, voids, impurities, high-density dislocations, stacking faults, chemical segregation, and surface flaws [15], [16]. Such defects, specifically nanocracks, have been shown as a leading cause of lithium intrusion into the SE [17]. At the macroscale, Kim *et al.* showed that changing the density of cubic LLZO results in significant changes in fracture toughness and hardness [14]. Hu *et al.* also presented the effect of relative density on the bulk properties of Ta-doped LLZO pellets, reporting disparate mechanical properties for pellets with varying densities [18].

This work reports the first compressive strength measurement of Al-substituted LLZO and investigates microscale spatial variations in mechanical properties of LLZO SE using instrumented indentation testing. Microscale pillars were milled *via* focused ion beam (FIB) milling at various locations across a SE pellet and compressed until failure using a flat punch (Figure 1e, f). Failure modes of the ceramic pillars are shown to be axial splitting, top surface splitting, shearing, and complete failure across/through grain boundaries due to crack propagation, where all failure modes result in cracking parallel to the compressive force (Figure

1c, d). The results show a surprising degree of correlated variation in Young's modulus and compressive strength across the SE—variations that to-date have remained undetected or unreported through macroscale property testing alone. Attributing such variations to specific process-structure causes is an important but challenging endeavor. In this work, we attempt a preliminary explanation of the observed process variations by: 1) fitting a linear model relating Young's modulus and compressive strength across all measurements, and 2) conducting molecular dynamics (MD) simulations of LLZO with voids (porosity) representing localized defects in the pillars. The results indicate the importance of compressive strength as a mechanical property of interest for LLZO and the importance of characterizing mechanical properties of SEs at the microscale.
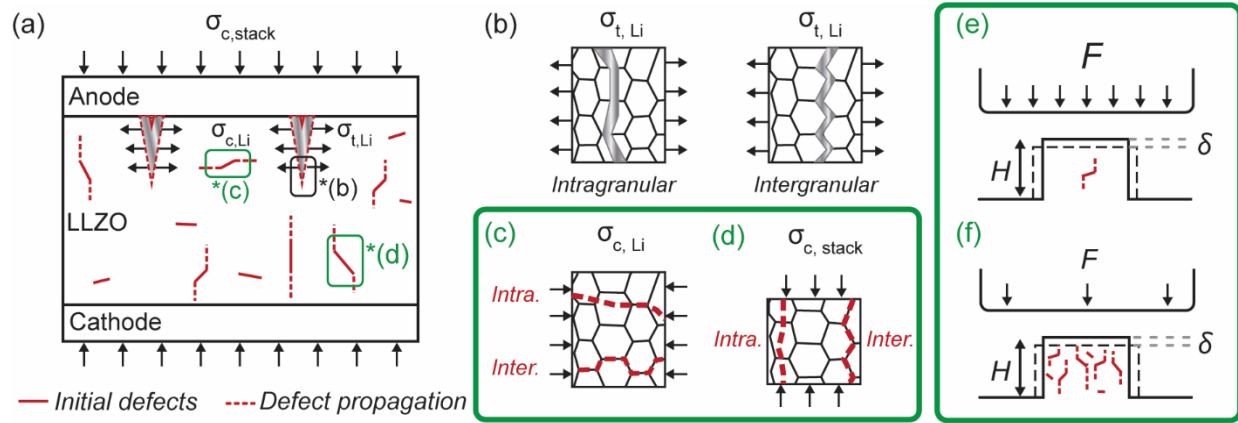
Figure 1. SE stress states and failure modes in all-solid-state lithium metal batteries. a) Conceptual illustration of tensile ($\sigma_{t,\,Li}$) and compressive (Li: $\sigma_{c,\,Li}$; stack: $\sigma_{c,\,stack}$) stresses within the SE. Initial defects (red solid lines) propagate as a result of these stresses (red dashed lines). (b-d) Magnified views of regions indicated in (a). b) LLZO failure in tension arises due to Li intrusion and may be intra- or intergranular. c, d) This study investigates LLZO in compression. Compressive failure in ceramics arises from intra- or intergranular crack propagation in a direction parallel to the applied stress. e, f) Pillar compression using a flat punch provides a controlled means of investigating compressive stress states in LLZO. While the compressive strength of LLZO changes with defect density (represented by large and small values of applied load, F), we observe a constant failure strain $\varepsilon_Y = \delta/H$.

Methods

    LLZO Preparation

LLZO solid electrolyte pellets were prepared with purchased Al-substituted LLZO powder

($Li_{6.25}Al_{0.25}La_3Zr_2O_{12}$) from Ampcera having an average grain size of 500 nm. This material is

cubic at room temperature [19]. Al-substituted LLZO powder was mixed with 5 wt% MgO

nanopowder (50 nm) and 5 wt% Li_2CO_3. MgO nanopowder was used to suppress abnormal grain

growth during sintering [20], [21]. Li_2CO_3 was used to offset lithium loss during sintering.

Mixed powder (0.5 g) was put into a die and pressed with 150 MPa of force for 30 s. After

removal from the die, green pellets were placed in a tube furnace and heated to 1200 °C for 4

hours under Ar atmosphere. Fully prepared pellets had a diameter of 14.9 mm and a thickness of

0.74 mm. X-ray diffraction (XRD) was completed with a Bruker D2 Phaser to confirm cubic

phase stability 24 hours after sintering. Relative density was estimated by measuring the volume

and weight of a pellet. Samples were stored in an LC Technology glovebox (H_2O, $O_2 < 0.1$ ppm)

to reduce oxidation and surface contamination. Ionic conductivity of an LLZO pellet of known

area was measured after coating both sides of the pellet with gold. Gold sputtering was done at

30 mA for 120 s. Electrochemical impedance spectroscopy (EIS) was conducted using point

contacts on each side of the pellet with a Bio-Logic VSP-300 potentiostat over a frequency range

of 0.1 Hz to 7 MHz. Ionic conductivity was determined from the intercept of the high-frequency

semi-circle with the x-axis (Table S2). Symmetric cells were assembled with the LLZO pellet to

report cycling performance and critical current density. Symmetric cells were assembled with

gold-coated LLZO pellets. Lithium metal was then melted on the pellets at 200 °C in an Ar-filled

glovebox. Cells were assembled in a 2032 coin cell case pressed with an MSE PRO hydraulic

manual crimper.

Instrumented Indentation Testing

LLZO SE was prepared for mechanical property characterization by dry polishing the top surface until an average surface roughness (Ra) of ~10 nm was achieved. Surface roughness was measured using scanning probe microscopy with a Bruker Hysitron TI Premier nanoindenter. Pillars were milled into the top surface of the LLZO SE using a four-step concentric ring milling process with an FEI Helios Nanolab 650 dual beam FIB and scanning electron microscope (SEM). First, a volume for the punch to travel into the surface was created by milling a 30 µm outer diameter ring (inner diameter 12 µm) using a beam voltage of 30 keV and a current of 21 nA. Next, the pillar was refined with two more millings at 2.5 nA and 0.79 nA. Lastly, the pillar was milled at a current of 80 pA to minimize the taper angle. Pillars were visually inspected to ensure no surface artifacts or additional porosity were introduced during the milling process. Pillars were compressed with a 20 µm diameter flat punch tip using a Bruker Hysitron PI89 SEM Picoindenter stage loaded into an FEI Quanta 600F SEM. Pillars were located and indented using *in-situ* SEM imaging. Loading rates from 100 µN/s to 3500 µN/s were applied. Load-controlled indentation to pillar failure is a well-established method to determine the compressive strength of ceramics with instrumented indentation testing [22]-[24]. The loading/unloading curve was translated into an engineering stress-strain curve given the starting pillar diameter (measured at half the height of the pillar) and the pillar height. Pillar densification was neglected when calculating stress. Pillar compression experiments were performed on three LLZO pellets, with two testing sites located on each pellet. Testing sites were located at least 5 mm apart. At least four pillars were milled at each testing site, avoiding obvious surface porosity. During milling, transfer, and imaging, a number of pillars were compromised and could not be tested. Between one and four pillars were successfully tested to failure at each site.

Nanoindentation was completed using a Bruker Hysitron TI Premier nanoindenter to determine the Young's modulus and hardness of the LLZO pellet with a Berkovich tip. Tip calibration was completed periodically using a standard Si sample. Indentation allows for the reduced modulus to be calculated from the slope of the unloading curve and the tip area, which is derived from the tip function. The reduced modulus is the modulus measured taking into account the interaction of the tip and substrate on the response. Hardness was calculated from the maximum load applied and the tip area. Young's modulus for the SE was calculated knowing the reduced modulus, the Young's modulus of the indenter tip, and the Poisson's ratio of the tip and LLZO [25]. Nanoindentation results were averaged from more than 20 indentations across three different areas.

Molecular Dynamics Simulations

MD simulations of $Al_{0.25}Li_{6.25}La_3Zr_2O_{12}$ were conducted in LAMMPS [26] using the Buckingham-Coulomb interatomic potential with details provided in the Supporting Information (Table S3). The initial cubic LLZO crystalline structure consisted of a 188-atom unit cell obtained from quantum mechanical relaxation using VASP [27]-[30]. Subsequently, the unit cell was replicated in a $10 \times 10 \times 10$ arrangement, resulting in a structure containing 188,000 atoms. This structure was then equilibrated at 300 K and zero pressure with an NPT ensemble for 15 ps using LAMMPS. To study the effect of porosity on LLZO mechanical response, spherical voids of varying sizes were introduced into the relaxed LLZO model. Stoichiometry and electrical charge neutrality were maintained when removing atoms. Void-containing models were equilibrated at 300 K and zero pressure in the NPT ensemble for 10 ps to achieve stable configurations. Void volumes determined from these stable configurations were used to calculate porosity. All models were periodic in the X, Y, and Z directions. The resulting structures were

subjected to uniaxial loading until failure. A timestep of 1 fs and a strain rate of 10^9 s^{-1} were applied to all simulations. Nine models, with porosity ranging from 0 to 42.18%, were built and tested. OVITO was used for visualization and post-simulation analysis [31].

Results and Discussion

Material Characterization

Electrochemical testing and XRD measurements were used to confirm the SE properties of LLZO pellets undergoing mechanical testing. The Al-substituted LLZO pellets maintained their cubic structure after sintering, as shown from XRD results (Figure 2a). The cubic phase is desired due to its higher ionic conductivity [32]-[34], where ion migration pathways have shorter distances compared to the tetragonal phase [35]. The ionic conductivity of the LLZO pellets used in this study is 0.13 mS/cm, as calculated from EIS measurements (Figure 2b), which matches well with other literature values (Table S2). Symmetric cell electrochemical testing results (Figure 2c) show stable charge-discharge cycling up to a critical current density of 1.0 mA/cm^2, after which short-circuiting occurs due to lithium intrusion through the SE. The relative density of the full pellets was determined to be 96% given a weight and volume measurement (4.91 g/cm^3). After confirmation of the stable electrochemical performance of the LLZO SE used in this study, mechanical properties were characterized on pristine LLZO pellets.
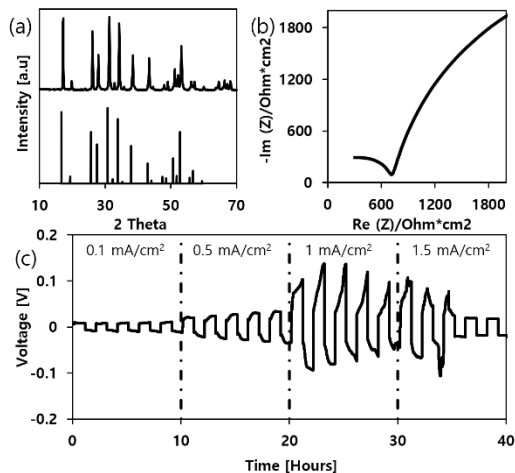
Figure 2. LLZO pellet characterization. a) XRD analysis of an LLZO pellet showing cubic phase stability at room temperature (C-LLZO Ref: ICSD (98-042-2259)). b) EIS Nyquist plot of LLZO. c) Cell voltage measurements obtained from cycling an LLZO pellet in a symmetric cell.

Instrumented indentation testing

Figure 3 illustrates the process of instrumented indentation testing by pillar compression (Figure 3a-d) and nanoindentation (Figure 3e-h). The geometry of pillar compression is shown schematically in Figure 3a. Important pillar parameters include the pillar taper angle (θ), the radius of curvature at the base (ρ), the height (H), and the diameter (D_0). The pillar compression experiment proceeds as follows: 1) pillars are located using *in-situ* SEM imaging (Figure 3b); 2) the flat punch tip is brought into contact with the pillar, ensuring that the pillar is centered in the middle of the flat punch tip and that the tip will not contact the bulk LLZO; 3) the pillar is loaded to a force below the expected fracture load, then unloaded at the same rate (Figure 3c); 4) the pillar is loaded and unloaded several times at varying loading rates (μN/s) with increasing maximum load until failure occurs. Figure 3d provides an example of the load-displacement curve to failure.

Using the described FIB milling process, the achieved pillars had measured diameters ranging from 2.5-3 μm and heights ranging from 6-8 μm. The relatively low aspect ratios were chosen to reduce the effects of bending during pillar compression. The resulting pillars are multi-grain, with ~3-6 grains present across the pillar diameter and ~12-16 grains along the height. Multi-grain pillars allow exploration of the effects of defects and grain-grain interactions on the mechanical properties of the SE. The taper angle was minimized to ~2° by successive annular milling. "Stopping and Range of Ions in Matter" (SRIM) [36] modeling was used to quantify the extent of gallium ion implantation during FIB milling of Al-substituted LLZO. At 0° incident angle, gallium ions will be implanted ~20 nm into the pillar surface; at 89° incident angle, ions will be implanted ~6 nm into the surface (Figure S1). Given the μm-scale pillar height and diameter, ion implantation is considered a surface effect that will not significantly impact the

measured results [37]. Using the method of pillar compression, the largest compressive strength measured was 2.63 GPa, corresponding to a Young's modulus of 150.97 GPa for the same pillar.

Nanoindentation provides a complementary measure of Young's modulus to that obtained by pillar compression, and the additional measure of hardness. In this work, nanoindentation of LLZO SE pellets was done with a Berkovich tip. The sharp tip indenter is brought to the surface of the material and loaded into the surface until a desired load is reached, after which the indenter is unloaded from the surface (Figure 3e-h). The unloading of the indenter allows for the elastic/plastic deformation of the material to be measured. Distinct from pillar compression, no pillars are milled in the nanoindentation experiment and the average depth of the tip displacement is much smaller, approximately 200 nm (Figure 3e). This shallow displacement means that nanoindentation is not as influenced by defects that may be present in the LLZO SE compared to pillar compression. Figure 3g shows a noticeable pile-up of LLZO after nanoindentation. Pile-up is caused by plastic flow of material upwards around the indenter due to strain hardening below the tip. A pile-up correction was applied and is described in the SI [38]. Nanoindentation of the same LLZO pellets tested by pillar compression provides a Young's modulus of ~145 GPa and a hardness of ~11.1 GPa (Table S1). The close agreement between nanoindentation and pillar compression results for Young's modulus and hardness indicates that size-dependent effects are unlikely for the pillar diameter used here [39].
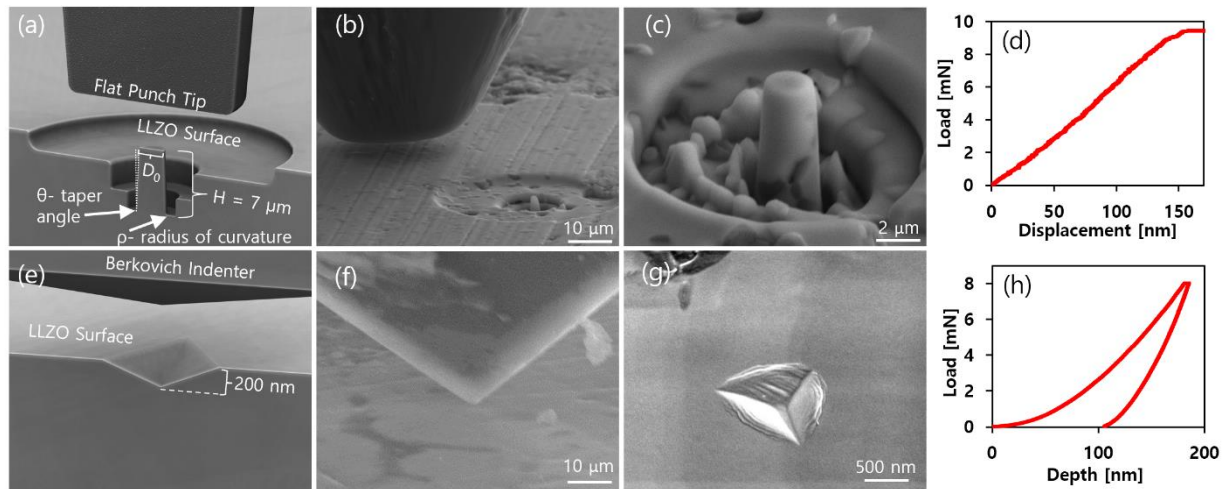
Figure 3. LLZO mechanical property measurement by micropillar compression (a-d) *vs.* nanoindentation (e-h). a) Cross-sectional schematic of pillar compression, with dimensional features of interest indicated. b) *In-situ* SEM image of a flat punch tip approaching a milled LLZO pillar. c) SEM image of milled pillar before compression. d) Load-displacement curve of a pillar compressed to failure. e) Cross-sectional schematic of Berkovich tip and surface deformation after indentation. f) *In-situ* SEM image of a cube corner indenter touching the surface of LLZO (Berkovich tip cannot be imaged *in-situ* with the SEM; a cube corner indenter image is provided here as a comparable reference image for the technique). g) SEM image of a Berkovich tip indentation on LLZO with pile-up present. h) Load-displacement curve of indentation on LLZO with Berkovich tip.

Figure 4 provides results of pillar compression loading/unloading experiments to failure. Load-displacement curves for varying loading rates are provided in Figure 4a. The load-displacement curves of each LLZO pillar after failure are translated into engineering stress-strain curves given the pillar's initial height and diameter at half height. The engineering stress-strain curves are presented in Figure 4b for all pillars loaded until failure.

Pillar compression provides three methods with which Young's modulus can be estimated: 1) from the average slope of multiple unloading stress-strain curves before failure; 2) from the linear elastic region of the pillar's stress-strain curve when loaded until failure; and 3) using Equation 1 to account for detailed pillar geometry, as presented in Yang *et al.* [40]. By estimating the Young's modulus from averaging the unloading curves (Method 1) it is assumed that elastic deformation of the flat punch tip is minimized. During some tests, the pillar would fail during the first loading, meaning the Young's modulus could not be estimated during the unloading. Predicting Young's modulus from the fracture curve (Method 2) is common in mechanics testing but may suffer inaccuracies from elastic compliance of the flat punch tip itself. Equation 1 considers non-idealities of pillar geometry when estimating Young's modulus, E, as:

$$E = \psi\left(1 + \frac{\pi(1-v)D_0}{8H}\right)\frac{4PH}{\pi D_0\big(D_0 + 2H tan(\theta)\big)\delta_t} \tag{1}$$

where D_0, H, and θ are as defined above (Figure 3a), δ_t is the pillar displacement under applied load P, and v is Poisson's ratio. The correction factor, ψ, is estimated given the pillar radius of curvature, top diameter, and height [40].

Figure 4c plots compressive strength *vs.* Young's modulus for all pillars loaded until failure. Compressive strength was recorded when catastrophic failure of the pillar occurred. Young's modulus was calculated using the methods described above and the results differentiated in

Figure 4c. A discussion comparing the results of all three methods is provided in the SI (Table S4), where all three methods, statistically, estimate the same values. The effect of loading rate on LLZO Young's modulus and compressive strength was evaluated using the variable loading rate data from Figure 4a. Both properties were determined to be independent of loading rate (Figure S2).
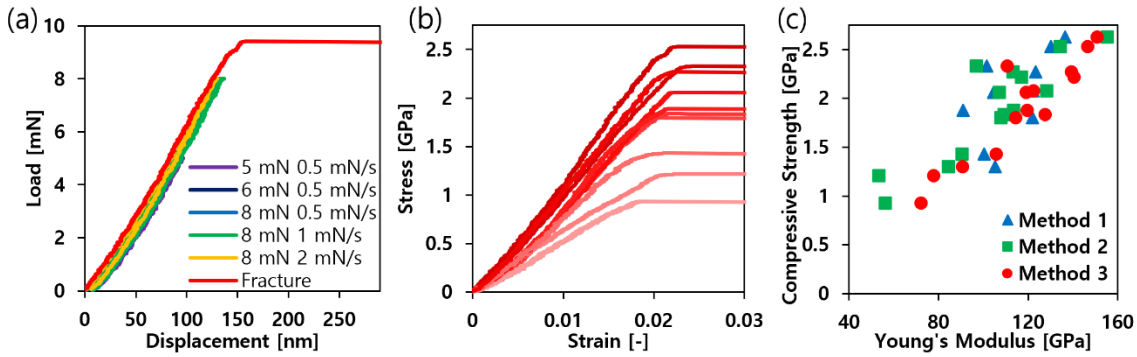
Figure 4. Pillar compression procedure and results. a) Load-displacement graph showing standard procedure for determining the compressive strength and rate dependency of a single FIB milled LLZO pillar. b) Stress-strain curves of all fractured pillars showing variable fracture stress and a consistent failure strain across all pillars. c) Compressive strength of fractured pillars plotted against the pillar's respective Young's modulus, with the three methods for estimating the Young's modulus plotted: Method 1 (averaged from unloading), Method 2 (loading to failure), Method 3 (Equation 1).

The results of Figure 4 display several noteworthy features. First and foremost is the large range of strength (0.93-2.63 GPa) and Young's modulus (72.1-150.97 GPa) values measured. A high degree of variability in compressive strength and Young's modulus occurred routinely within a single test site of one pellet, meaning that two pillars directly next to each other would produce different mechanical properties (Figure S3). This indicates that mechanical property variations between pillars are due to structural changes of the LLZO SE across small length scales. The second noteworthy feature is the single, strong linear relationship between compressive strength and Young's modulus values observed across multiple areas and multiple pellets (Figure 4c), with a regression model for the two variables resulting in a significant relationship ($F_{1,12} = 45.85$, $p < 0.001$). Finally, we note that all pillars tested have nearly identical failure strain, despite large differences in failure stress. When comparing all stress-strain curves for the fractured pillars (Figure 4b), the average strain at failure is measured to be $2.2 \pm 0.3\%$. Compressive strength tests are often plagued with variance and uncertainty due to complex failure modes [41]. In cases where the results are highly influenced by variations in failure mode geometry and/or loading methods, we would expect large differences in failure strain across tests. The fact that all compression tests shown here have statistically the same failure strain indicates that the observed differences in failure stress of each pillar are likely pillar dependent, not method dependent. Interestingly, this result also indicates that all LLZO pillars tested here fail under approximately the same amount of deflection. Overall, these features of the results indicate that the large variance in compressive strength observed could be due to microscale variations between pillars, particularly defects, with more defects reducing the stress needed to reach the failure strain.

SEM images obtained during pillar compression provide further insight into failure modes and crack initiation/propagation in LLZO. LLZO used in this study shows the tendency for axial

splitting, top surface splitting, shearing, and complete failure across/through grain boundaries due to crack propagation. Axial splitting occurs when angled slip planes intersect at some depth of the pillar where a crack will initiate due to increased stress concentrations at that location (Figure 5a) [42]. Top surface splitting occurs perpendicular to slip planes, where cracks originate at the flat punch tip interface and cause parallel cracks to travel down the height of the pillar (Figure 5b) [42]. Shearing, or diagonal splitting, may be caused by a shear plane existing within the pillar at some angle. Maximum shear stress occurs along this plane, resulting in failure and the release of material from the pillar [43]. The observed failure modes arise from the brittle nature of LLZO. Strong covalent bonds prohibit plastic flow across slip planes, resulting in cracking and chipping before catastrophic failure. SEM imaging of one LLZO pillar before compression shows significant microscale porosity present below the top surface (Figure 5c). FIB cross-sectional analysis of another pillar after compressive failure shows internal porosity and cracks present (Figure 5d). Such defects do not arise from the FIB milling process, as shown through SEM imaging of a straight-milled trench (Figure S4). In ceramics, porosity acts as an internal defect providing a crack launch site [44], and can be a major contributor to premature failure in compression. During compression, almost all cracking occurs parallel to the force applied, regardless of slip plane orientation. Additionally, both intra- and intergranular cracking is apparent after pillar fracture has occurred, as shown in Figure S5. The failure modes observed here present a major risk for through-cracking and short circuiting of the SE, given a crack-propagation-based model of lithium intrusion [45].
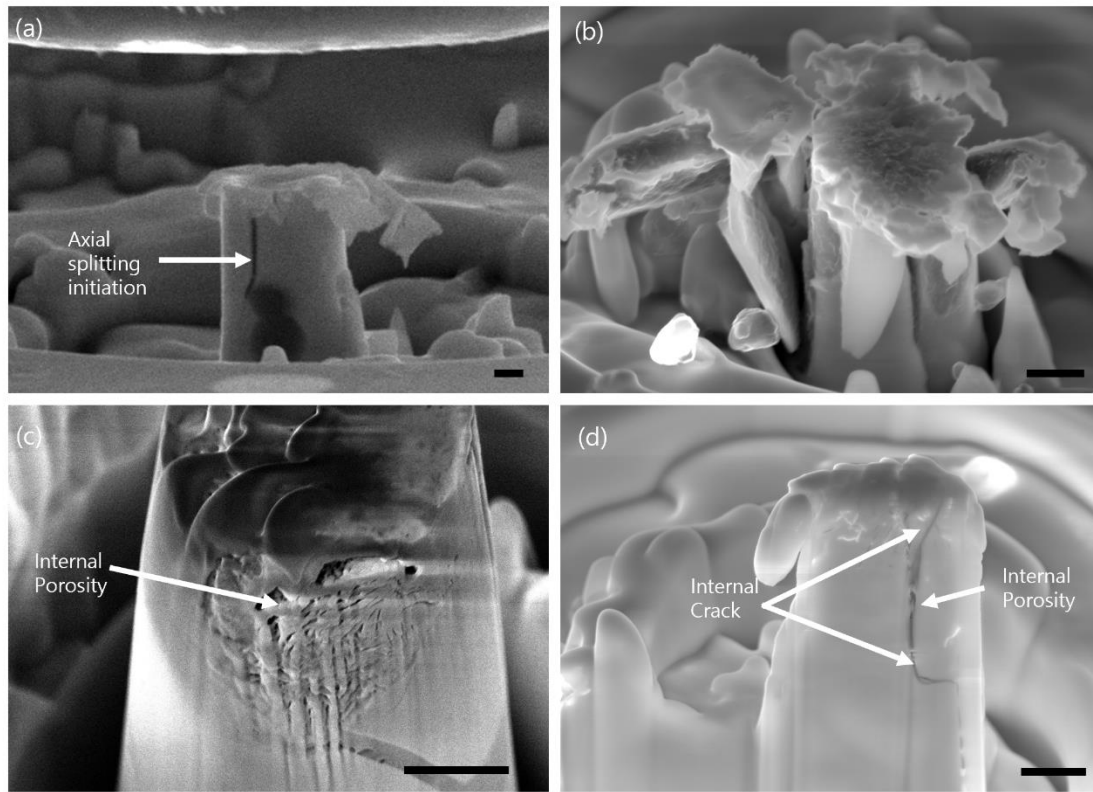
Figure 5. Failure modes and defects observed in LLZO pillars. a) Axial splitting of LLZO pillar. b) Top splitting of LLZO pillar. c) A pristine (unloaded) pillar showing internal porosity. d) A pillar cross-section (FIB-milled) after compression showing the presence of internal porosity and cracks generated from the defect. All scale bars are 1 μm.

Effective Microscale Porosity Model

Identifying specific causes of premature failure for ceramics in compression is notoriously difficult, as evidenced by the multiplicity of LLZO failure modes observed in pillar compression experiments (Figure 5). Equation 2 has been presented in the literature to provide an estimate of Young's modulus reduction as a function of material porosity, *x*:

$$E = E_0 e^{-bx} \tag{2}$$

where E_0 is the nonporous Young's modulus and *b* is an empirical fitting parameter [46]. This equation, fit to our experimental data, provides an estimate of the effective porosity, *i.e.* effective loss of LLZO material strength, required to produce the wide range of Young's modulus and compressive strength measurements observed. In the case of microscale pillar compression measurements, it is not possible to experimentally measure localized LLZO porosity at each compression site. Instead, we rely on MD simulations to predict *E* as a function of effective porosity, *x*, and estimate an appropriate fitting parameter *b*. MD simulations were chosen to capture the surface effects of nanovoids that would be left undetected by continuum-scale computational approaches. In the absence of the ability to effectively simulate multiple types of defects that may be present in a single pillar, effective porosity is used to represent the general loss of material strength that occurs with reduced cross-sectional area and the introduction of stress concentrations, thus modeling general effects similar to those caused by types of defects other than pores. In addition to porosity, there could be other factors contributing to reduced Young's modulus, such as grain boundaries and impurities. However, porosity is likely dominant, especially considering the >50% reduction in Young's modulus and compressive strength demonstrated in Figure 4c.

Porosity in MD simulations was represented as a spherical void in the center of a material model periodic in x, y, and z directions (Figure 6a), with the void volume *vs.* total volume set to match the target effective porosity. Since the models are periodic in all directions, they stand for bulk material with the same volume percentage of unconnected voids. Stress-strain curves were generated by uniaxially compressing the simulation volume in one direction and relaxing the other two directions to achieve a stress-free state (Figure 6b). From stress-strain curves, we calculated Young's modulus (E) and compressive strength (σ) for models with porosity and normalized their values with simulated pristine LLZO Young's modulus (E_0) and compressive strength (σ_0), respectively. Fitting these data to Equation 2 yields a value for *b* of 1.919 as listed in Table 1.

Simulated values of normalized Young's modulus and compressive strength can be compared with experimental values given experimental estimates of E_0 and σ_0. We obtain the former from nanoindentation, a surface measurement less sensitive to defects and voids, providing an $E_0 \sim$ 145 GPa. This value aligns well with the largest Young's modulus measured by pillar compression (E_0 = 150.97 GPa), as well as literature values provided in Table S1. We take the compressive strength of this same pillar, 2.63 GPa (the largest compressive strength measured) to be an estimated lower bound for σ_0. A plot of normalized Young's modulus *vs.* normalized compressive strength shows good agreement between simulation and experiment (Figure 6c).

Figure 6d plots simulation and experimental values of E/E_0 *vs.* effective porosity, *x*. Plotted simulation values were obtained directly from MD results; plotted experimental values come from fitting measured Young's modulus values to the porosity model (Equation 2) using b = 1.919 and an E_0 = 150.97 GPa to determine an effective localized porosity value (*x*) for each value. Plotting each pillar's effective porosity with its compressive strength, we obtain Figure 6e.

The results of both analyses show good agreement between computational and experimental data, indicating that microscale porosity and other defects that may produce effects similar to those described by Equation 2 are the cause of the wide range of Young's modulus and compressive strength values in LLZO.

The strength of such an analysis lies in the ability to relate a localized LLZO effective porosity change to a predicted change in mechanical properties. For example, our computational model indicates an effective porosity of 10% results in a 17.5% decrease in Young's modulus. Sandt *et al.* reported a similar result for LLZO Young's modulus using *ab initio* simulations, concluding that a porosity of 10% results in a 27% decrease in Young's modulus [47]. Fitting our experimental results to the porosity model derived from MD simulations enables the large range of experimental Young's modulus (150.97- 72.1 GPa) being accounted for by a localized (*i.e.* microscale) porosity range of 0-38.5%. It is important to note that our results consider localized (*i.e.* microscale) variations in material strength. While porosity values up to 38.5% are unlikely for bulk LLZO, such material strength reductions are conceivable in localized regions at μm scale and when other defects that contribute to increased effective porosity are considered. It is important to recognize limitations in porosity-based simulations in the limit of high porosity *(e.g.* > 25%) [46]. In such cases, pore geometry and pore-pore interactions can have significant effects on the results. To examine the extent of pore-pore interactions in LLZO pellets used in this work, we obtained a cross-sectional SEM image of a polished pellet (Figure S6). Microscale voids present in the cross-sectional view show well-dispersed porosity, suggesting limited pore-pore interactions in experimental LLZO samples. The nature of the porosity inclusion on MD simulation results was briefly explored, where it was observed that one void region or multiple void regions had an insignificant effect on the mechanical response as long as the same porosity

volume was used. In cases where high porosities are required to account for large reductions in Young's modulus or compressive strength, further modeling of the effects of other types of defects (*e.g.* cracks, impurities, etc.) on the mechanical response of LLZO may be needed to account for the observed property changes.
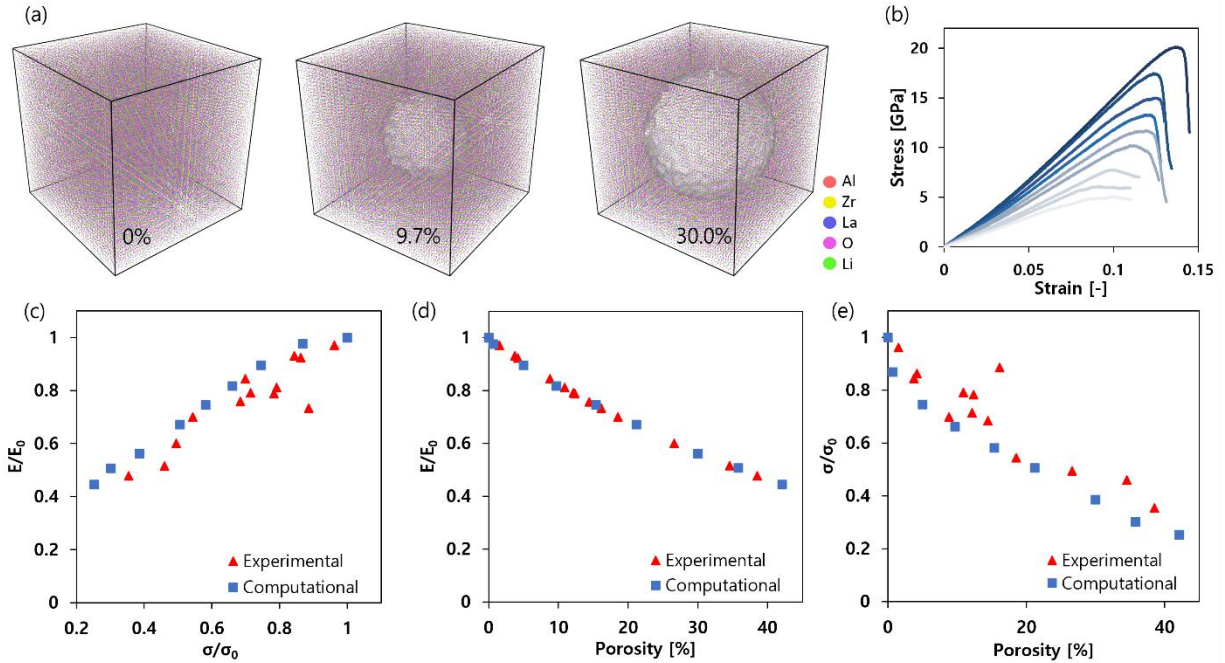
Figure 6. **MD simulation results and comparison with experiment.** a) MD simulations showing representative introduced porosities of 0%, 9.7%, and 30.0%. b) Stress-strain curves of simulated results. The gradient from dark to light blue indicates increasing porosity. c) Normalized Young's modulus *vs.* normalized compressive strength results from experiment and MD simulations. d) Normalized Young's modulus *vs.* porosity, with experimental Young's modulus values fitted to the Equation 2 porosity model. e) Normalized compressive strength *vs.* porosity. The porosity is either simulated pores (MD) or effective porosity (experimental).

Table 1: Porosity model (Equation 2) fitting parameters derived from MD simulations.

	E_0	-b	95% Confidence Interval of -b	R^2
Computational	136.6	1.919	(1.87 – 1.969)	0.9985
Experimental	150.97	1.919	-	-

Conclusions

Experimental measurements of LLZO compressive strength and Young's modulus by pillar compression indicate surprising variability in the mechanical properties of SE pellets across micrometer length scales. Highest measured values of Young's modulus by pillar compression agree well with literature reports for bulk LLZO, as well as our own measurements of the same SE pellet by nanoindentation. The results indicate that a pristine LLZO pillar, with no defects present, has a compressive strength of ~2.63 GPa. As defect density increases, however, the compressive strength of LLZO will decrease. A reduction in compressive strength of nearly 65%, to 0.93 GPa, was observed, with a corresponding decrease in Young's modulus from 150.97 to 72.1 GPa.

The wide range of localized mechanical properties in LLZO may explain the non-uniform plating and stripping in LLZO-based solid-state batteries. We presume that the least resilient pillars correlate with preferential sites for mechanical degradation or Li intrusion. Therefore, complete characterization of LLZO SE should include pillar compression or other microscale techniques to assess the weakest local areas in a bulk specimen. Conventional techniques that measure average mechanical properties are insufficient to capture the local variation that likely dictates ultimate robustness of LLZO in a battery. An initial theory explaining the high variance of experimentally measured mechanical properties based on microscale variations in each pillar (i.e. defects)–represented quantitatively by an effective porosity value–produces good agreement with experimental data. Additionally, our experimental results reveal a nearly constant failure strain across different areas in different LLZO SE samples, even though their compressive strengths varied significantly. Larger porosity means larger surface areas, which provide more opportunities for cracks to initiate and further leads to fracture. Therefore, porosity induces two

deformation mechanisms within LLZO: one is the densification process which can lead to a larger strain compared to void-free LLZO; the other is the crack initiation process making the failure happen earlier compared to void-free LLZO. The competition between the two mechanisms appears to reach a balance at a consistent value of uniaxial strain. Future experimental and computational work would do well to study LLZO in complex loading conditions to better understand the consistent failure strain observed here and simulate polycrystalline LLZO in compression with different grain sizes. The current interatomic potential for LLZO makes such simulations prohibitively expensive. Therefore, we leave it to future MD simulation work to computationally elucidate the interactions among porosities, defects, grain boundaries, and fracture.

Jaron V. Moon – Conceptualization, Data curation, Formal Analysis, Investigation, Project Administration, Visualization, Supervision Writing - original draft, review, and editing

Md Takmil Sakir – Investigation, Data curation, Formal Analysis, Methodology, Software, Visualization, Writing – review and editing

Wooseok Go – Investigation, Data curation, Formal Analysis, Resources, Visualization, Writing – review and editing

Rui Xie – Investigation, Software, Formal Analysis

Michael C. Tucker – Funding acquisition, Resources, Supervision, Writing – review and editing

Marca Doeff – Funding acquisition, Resources, Supervision, Writing – review and editing

Haoran Wang – Funding acquisition, Software, Resources, Supervision, Writing – review and editing

Roseanne Warren – Conceptualization, Funding Acquisition, Supervision, Writing – review and editing

References

[1] K. J. Kim, M. Balaish, M. Wadaguchi, L. Kong, and J. L. M. Rupp, 'Solid-State Li–Metal Batteries: Challenges and Horizons of Oxide and Sulfide Solid Electrolytes and Their Interfaces', *Adv Energy Mater*, vol. 11, no. 1, pp. 1–63, 2021, doi: 10.1002/aenm.202002689.

[2] F. Aguesse *et al.*, 'Investigating the dendritic growth during full cell cycling of garnet electrolyte in direct contact with Li metal', *ACS Appl Mater Interfaces*, vol. 9, pp. 3808–3816, 2017, doi: 10.1021/acsami.6b13925.

[3] L. C. De Jonghe, L. Feldman, and A. Buechele, 'FAILURE MODES OF NA-BETA ALUMINA', *Solid State Ion*, vol. 5, pp. 267–269, 1981, [Online]. Available: https://escholarship.org/uc/item/2jp514j2

[4] E. J. Cheng, A. Sharafi, and J. Sakamoto, 'Intergranular Li metal propagation through polycrystalline Li6.25Al0.25La3Zr2O12 ceramic electrolyte', *Electrochim Acta*, vol. 223, pp. 85–91, 2017, doi: 10.1016/j.electacta.2016.12.018.

[5] X. Liu *et al.*, 'Local electronic structure variation resulting in Li "filament" formation within solid electrolytes', *Nat Mater*, vol. 20, no. 11, pp. 1485–1490, 2021, doi: 10.1038/s41563-021-01019-x.

[6] S. Kalnaus, N. J. Dudney, A. S. Westover, E. Herbert, and S. Hackney, 'Solid-state batteries: The critical role of mechanics', *Science (1979)*, vol. 381, p. eabg5998, 2023, doi: 10.1126/science.abg5998.

[7] J. Hu *et al.*, '3D stress mapping reveals the origin of lithium-deposition heterogeneity in solid-state lithium-metal batteries', *Cell Rep Phys Sci*, vol. 3, p. 100938, 2022, doi: 10.1016/j.xcrp.2022.100938.

[8] F. Zhang *et al.*, 'A review of the effect of external pressure on all-solid-state batteries', *eTransportation*, vol. 15, p. 100220, 2023, doi: 10.1016/j.etran.2022.100220.

[9] W. Zaman *et al.*, 'Temperature and Pressure Effects on Unrecoverable Voids in Li Metal Solid-State Batteries', *ACS Appl Mater Interfaces*, vol. 15, pp. 37401–37409, 2023, doi: 10.1021/acsami.3c05886.

[10] X. Ke, Y. Wang, G. Ren, and C. Yuan, 'Towards rational mechanical design of inorganic solid electrolytes for all-solid-state lithium ion batteries', *Energy Storage Mater*, vol. 26, pp. 313–324, 2020, doi: 10.1016/j.ensm.2019.08.029.

[11] S. Yu *et al.*, 'Elastic Properties of the Solid Electrolyte Li7La3Zr2O12 (LLZO)', *Chemistry of Materials*, vol. 12, pp. 197–206, 2016, doi: 10.1021/acs.chemmater.5b03854.

[12] J. E. Ni, E. D. Case, J. S. Sakamoto, E. Rangasamy, and J. B. Wolfenstine, 'Room temperature elastic moduli and Vickers hardness of hot-pressed LLZO cubic garnet', *J Mater Sci*, vol. 47, pp. 7978–7985, 2012, doi: 10.1007/s10853-012-6687-5.

[13] A. Wang, J. F. Nonemacher, G. Yan, M. Finsterbusch, J. Malzbender, and M. Krüger, 'Mechanical properties of the solid electrolyte Al-substituted Li7La3Zr2O12(LLZO) by

utilizing micro-pillar indentation splitting test', *J Eur Ceram Soc*, vol. 38, pp. 3201–3209, 2018, doi: 10.1016/j.jeurceramsoc.2018.02.032.

[14]   Y. Kim, H. Jo, J. L. Allen, H. Choe, J. Wolfenstine, and J. Sakamoto, 'The Effect of Relative Density on the Mechanical Properties of Hot-Pressed Cubic Li 7 la 3 Zr 2 O 12', *Journal of the American Ceramic Society*, vol. 99, no. 4, pp. 1367–1374, Apr. 2016, doi: 10.1111/jace.14084.

[15]   X. L. Phuah, J. Cho, T. Tsakalakos, A. K. Mukherjee, H. Wang, and X. Zhang, 'Defects in flash-sintered ceramics and their effects on mechanical properties', *MRS Bull*, vol. 46, pp. 44–51, 2021, doi: 10.1557/s43577-020-00014-y.

[16]   J. D. Hogan, L. Farbaniec, T. Sano, M. Shaeffer, and K. T. Ramesh, 'The effects of defects on the uniaxial compressive strength and failure of an advanced ceramic', *Acta Mater*, vol. 102, pp. 263–272, 2016, doi: 10.1016/j.actamat.2015.09.028.

[17]   G. McConohy *et al.*, 'Mechanical regulation of lithium intrusion probability in garnet solid electrolytes', *Nat Energy*, vol. 8, p. 423, 2023, doi: 10.1038/s41560-022-01186-4.

[18]   S. Hu, P. Xu, L. S. De Vasconcelos, L. Stanciu, H. Ni, and K. Zhao, 'Elastic Modulus, Hardness, and Fracture Toughness of Li6.4La3Zr1.4Ta0.6O12Solid Electrolyte', *Chinese Physics Letters*, vol. 38, no. 9, p. 098401, 2021, doi: 10.1088/0256-307X/38/9/098401.

[19]   S. Mukhopadhyay *et al.*, 'Structure and stoichiometry in supervalent doped Li7La3Zr2O12', *Chemistry of Materials*, vol. 27, pp. 3658–3665, 2015, doi: 10.1021/acs.chemmater.5b00362.

[20]   H. Guo *et al.*, 'Achieving high critical current density in Ta-doped Li7La3Zr2O12/MgO composite electrolytes', *J Alloys Compd*, vol. 856, p. 157222, 2021, doi: 10.1016/j.jallcom.2020.157222.

[21]   R. A. Jonson, E. Yi, F. Shen, and M. C. Tucker, 'Optimization of Tape Casting for Fabrication of Li6.25Al0.25La3Zr2O12Sheets', *Energy and Fuels*, vol. 35, pp. 8982–8990, 2021, doi: 10.1021/acs.energyfuels.1c00566.

[22]   M. D. Uchic and D. M. Dimiduk, 'A methodology to investigate size scale effects in crystalline plasticity using uniaxial compression testing', *Materials Science and Engineering: A*, vol. 400–401, pp. 268–278, 2005, doi: 10.1016/j.msea.2005.03.082.

[23]   E. Camposilvan and M. Anglada, 'Size and plasticity effects in zirconia micropillars compression', *Acta Mater*, vol. 103, pp. 882–892, 2016, doi: 10.1016/j.actamat.2015.10.047.

[24]   H. Fei, A. Abraham, N. Chawla, and H. Jiang, 'Evaluation of micro-pillar compression tests for accurate determination of elastic-plastic constitutive relations', *Journal of Applied Mechanics, Transactions ASME*, vol. 79, no. 6, pp. 1–9, 2012, doi: 10.1115/1.4006767.

[25]   R. Xu, H. Sun, L. S. de Vasconcelos, and K. Zhao, 'Mechanical and Structural Degradation of LiNi x Mn y Co z O 2 Cathode in Li-Ion Batteries: An Experimental Study', *J Electrochem Soc*, vol. 164, no. 13, pp. A3333–A3341, 2017, doi: 10.1149/2.1751713jes.

[26] A. P. Thompson *et al.*, 'LAMMPS - a flexible simulation tool for particle-based materials modeling at the atomic, meso, and continuum scales', *Comput Phys Commun*, vol. 271, p. 108171, 2022, doi: 10.1016/j.cpc.2021.108171.

[27] G. Kresse and J. Hafner, 'Ab initio molecular dynamics for liquid metals', *Phys Rev B*, vol. 47, no. 1, pp. 558–561, 1993, doi: 10.1103/PhysRevB.47.558.

[28] G. Kresse and J. Furthmüller, 'Efficient iterative schemes for ab initio total-energy calculations using a plane-wave basis set', *Journal of Physical Chemistry A*, vol. 54, no. 16, pp. 169–186, 1996, doi: 10.1021/acs.jpca.0c01375.

[29] G. Kresse and D. Joubert, 'From ultrasoft pseudopotentials to the projector augmented-wave method', *Phys Rev B Condens Matter Mater Phys*, vol. 59, no. 3, pp. 1758–1775, 1999, doi: 10.1103/PhysRevB.59.1758.

[30] G. Kresse and J. Furthmüller, 'Efficiency of ab-initio total energy calculations for metals and semiconductors using a plane-wave basis set', *Comput Mater Sci*, vol. 6, pp. 15–50, 1996, doi: 10.1016/0927-0256(96)00008-0.

[31] A. Stukowski, 'Visualization and analysis of atomistic simulation data with OVITO-the Open Visualization Tool', *Model Simul Mat Sci Eng*, vol. 18, p. 015012, 2010, doi: 10.1088/0965-0393/18/1/015012.

[32] K. Meier, T. Laino, and A. Curioni, 'Solid-state electrolytes: Revealing the mechanisms of Li-Ion conduction in tetragonal and cubic LLZO by first-principles calculations', *Journal of Physical Chemistry C*, vol. 118, pp. 6668–6679, 2014, doi: 10.1021/jp5002463.

[33] E. Rangasamy, J. Wolfenstine, J. Allen, and J. Sakamoto, 'The effect of 24c-site (A) cation substitution on the tetragonal-cubic phase transition in Li7-xLa3-xAxZr 2O12 garnet-based ceramic electrolyte', *J Power Sources*, vol. 230, pp. 261–266, 2013, doi: 10.1016/j.jpowsour.2012.12.076.

[34] F. Langer, J. Glenneberg, I. Bardenhagen, and R. Kun, 'Synthesis of single phase cubic Al-substituted Li7La3Zr2O12 by solid state lithiation of mixed hydroxides', *J Alloys Compd*, vol. 645, pp. 64–69, 2015, doi: 10.1016/j.jallcom.2015.03.209.

[35] J. Awaka, A. Takashima, K. Kataoka, N. Kijima, Y. Idemoto, and J. Akimoto, 'Crystal structure of fast lithium-ion-conducting cubic Li 7La3Zr2O12', *Chem Lett*, vol. 40, pp. 60–62, 2011, doi: 10.1246/cl.2011.60.

[36] J. F. Ziegler, M. D. Ziegler, and J. P. Biersack, 'SRIM - The stopping and range of ions in matter (2010)', *Nucl Instrum Methods Phys Res B*, vol. 268, pp. 1818–1823, 2010, doi: 10.1016/j.nimb.2010.02.091.

[37] J. A. El-Awady, C. Woodward, D. M. Dimiduk, and N. M. Ghoniem, 'Effects of focused ion beam induced damage on the plasticity of micropillars', *Phys Rev B Condens Matter Mater Phys*, vol. 80, p. 104104, 2009, doi: 10.1103/PhysRevB.80.104104.

[38]   P. Zhu, Y. Zhao, S. Agarwal, J. Henry, and S. J. Zinkle, 'Toward accurate evaluation of bulk hardness from nanoindentation testing at low indent depths', *Mater Des*, vol. 213, p. 110317, 2022, doi: 10.1016/j.matdes.2021.110317.

[39]   C. P. Frick, B. G. Clark, S. Orso, A. S. Schneider, and E. Arzt, 'Size effect on strength and strain hardening of small-scale [1 1 1] nickel compression pillars', *Materials Science and Engineering: A*, vol. 489, pp. 319–329, 2008, doi: 10.1016/j.msea.2007.12.038.

[40]   Y. Yang, J. C. Ye, J. Lu, F. X. Liu, and P. K. Liaw, 'Effects of specimen geometry and base material on the mechanical behavior of focused-ion-beam-fabricated metallic-glass micropillars', *Acta Mater*, vol. 57, pp. 1613–1623, 2009, doi: 10.1016/j.actamat.2008.11.043.

[41]   M. Iskander and N. Shrive, 'The effect of the shape and size of initial flaws on crack propagation in uniaxially compressed linear brittle materials', *Theoretical and Applied Fracture Mechanics*, vol. 109, p. 102742, 2020, doi: 10.1016/j.tafmec.2020.102742.

[42]   P. R. Howie, S. Korte, and W. J. Clegg, 'Fracture modes in micropillar compression of brittle crystals', *J Mater Res*, vol. 27, no. 1, pp. 141–151, 2012, doi: 10.1557/jmr.2011.256.

[43]   R. Shahrin and C. P. Bobko, 'Micropillar compression investigation of size effect on microscale strength and failure mechanism of Calcium-Silicate-Hydrates (C-S-H) in cement paste', *Cem Concr Res*, vol. 125, p. 105863, 2019, doi: 10.1016/j.cemconres.2019.105863.

[44]   A. A. Griffith, 'The phenomena of rupture and flow in solids', *Philos Trans R Soc Lond*, vol. 221, pp. 163–198, 1921, doi: 10.1098/rsta.1921.0006.

[45]   C. D. Fincher *et al.*, 'Controlling dendrite propagation in solid-state batteries with engineered stress', *ChemRxiv*, vol. 6, pp. 2794–2809, 2022, doi: 10.1016/j.joule.2022.10.011.

[46]   J. Luo and R. Stevens, 'Porosity-dependence of elastic moduli and hardness of 3Y-TZP ceramics.', *Ceram Int*, vol. 25, pp. 281–286, 1999, doi: https://doi.org/10.1016/S0272-8842(98)00037-6.

[47]   R. Sandt, Y. Wang, and R. Spatschek, 'Investigation of mechanical properties of garnet structured Li7La3Zr2O12 under Al3+ and Ta5+ co-substitutions', *Solid State Ion*, vol. 402, p. 116364, 2023, doi: 10.1016/j.ssi.2023.116364.